Analysis of a Lower-Tropospheric Gravity Wave Train Using Direct and Remote Sensing Measurement Systems

BENJAMIN A. TOMS[a]

School of Meteorology, University of Oklahoma, Norman, Oklahoma

JESSICA M. TOMASZEWSKI

Department of Atmospheric and Oceanic Sciences, University of Colorado Boulder, Boulder, Colorado

DAVID D. TURNER[b] AND STEVEN E. KOCH

National Severe Storms Laboratory, Norman, Oklahoma

(Manuscript received 8 June 2016, in final form 31 January 2017)

ABSTRACT

On 10 August 2014, a gravity wave complex generated by convective outflow propagated across much of Oklahoma. The four-dimensional evolution of the wave complex was analyzed using a synthesis of near-surface and vertical observations from the Oklahoma Mesonet and Atmospheric Radiation Measurement (ARM) Southern Great Plains networks. Two Atmospheric Emitted Radiance Interferometers (AERI)—one located at the ARM SGP central facility in Lamont, Oklahoma, and the other in Norman, Oklahoma—were used in concert with a Doppler wind lidar (DWL) in Norman to determine the vertical characteristics of the wave complex. Hydraulic theory was applied to the AERI-derived observations to corroborate the observationally derived wave characteristics.

It was determined that a bore-soliton wave packet initially formed when a density current interacted with a nocturnal surface-based inversion and eventually propagated independently as the density current became diffuse. The soliton propagated within an elevated inversion, which was likely induced by ascending air at the leading edge of the bore head. Bore and density current characteristics derived from the observations agreed with hydraulic theory estimates to within a relative difference of 15%. While the AERI did not accurately resolve the postbore elevated inversion, an error propagation analysis suggested that uncertainties in the AERI and DWL observations had a negligible influence on the findings of this study.

1. Introduction

Lower-tropospheric gravity waves are ubiquitous and often take the form of either internal bores or internal solitary waves. Such gravity waves may be generated by the disturbance of a surface-based inversion by density currents in the form of intense cold fronts (Smith et al. 1982; Karyampudi et al. 1995; Hartung et al. 2010), moist convective outflow (Knupp 2006; Coleman et al. 2009; Karan and Knupp 2009), sea-breeze fronts (Clarke et al. 1981; Sheng et al. 2009), or even by the interaction between convective outflow and sea-breeze fronts (Wakimoto and Kingsmill 1995; Kingsmill and Crook 2003). The vertical perturbation of the stably stratified layer generates an oscillatory motion that may propagate ahead of the wave source and be maintained if atmospheric wave ducting properties are present. This wave may take the form of either a bore, a solitary wave, or a packet of waves (Christie et al. 1979; Crook 1986; Rottman and Simpson 1989).

The passage of an atmospheric bore commonly instigates sustained modifications to the prewave environment (Clarke et al. 1981; Rottman and Simpson 1989; Koch et al. 1991). Initially, air near the surface is vertically displaced in advance of the bore head. The vertically displaced air cools adiabatically, creating a

[a] Current affiliation: Department of Atmospheric Science, Colorado State University, Fort Collins, Colorado.

[b] Current affiliation: NOAA/Earth System Research Laboratory, Boulder, Colorado.

Corresponding author: Benjamin A. Toms, ben.toms@colostate.edu

DOI: 10.1175/MWR-D-16-0216.1

compact column of relatively dense air aloft, allowing for an addition of mass in the total atmospheric column in the evacuated space. Additional mass transported by the bore contributes to the total increase of mass in the atmospheric column. Thus, an abrupt increase in surface pressure occurs as a result of bore passage, which is hydrostatically consistent with the magnitude of adiabatic cooling induced by the rising motion. The increased surface pressure gradient causes surface winds to increase in magnitude and rotate toward the direction of bore movement. On the back side of the bore head, downward mixing of horizontal momentum further increases the near-surface winds, while the downward mixing of potentially warmer air leads to a positive perturbation in surface temperature. Aside from pressure perturbations, which may be observed at the surface no matter the vertical placement of the wave, the influences of a solitary wave are similar to those of a bore, although they are transient and confined to the vertical region within which the solitary wave resides (Rottman and Einaudi 1993; Knupp 2006; Koch et al. 2008a).

The evolution of gravity wave complexes has been shown to be dependent upon the prewave kinematic and thermodynamic environment (Knupp 2006; Koch et al. 2008a,b). Atmospheric bores and solitons generated by density currents propagate within stable layers near the ground and are commonly confined to the lowest kilometers of the atmosphere (Rottman and Simpson 1989; Rottman and Grimshaw 2002). The vertical wind shear between two stably stratified layers may limit the vertical propagation of gravity waves, with winds orthogonal to the direction of wave propagation being the most conducive to wave ducting (Crook 1986, 1988; Rottman and Simpson 1989; Rottman and Einaudi 1993; Koch and Clark 1999). These physical relationships are mathematically explained via the Scorer parameter, defined here:

$$l^2(z) = \frac{N(z)^2}{[U(z) - C]^2} - \frac{[\partial^2 U(z)/\partial z^2]}{U(z) - C} \qquad (1)$$

where l^2 is the Scorer parameter, N is the Brunt–Väisälä frequency, U is the magnitude of the wind in the direction of bore propagation, and C is the propagation speed of the bore (Scorer 1949). The first term represents the contribution of stably stratified layers to wave-energy ducting, while the second represents the ducting induced by the curvature of the wind. Accordingly, the spatial characteristics of bores often vary substantially due to mesoscale variability in near-surface kinematic and thermodynamic characteristics (Hartung et al. 2010). The study of low-level atmospheric structure is therefore essential to understanding the evolution of such lower-tropospheric gravity waves.

The undular nature of a bore is dependent upon the ratio of the depth of the bore to the depth of the surface-based inversion (i.e., bore strength; $d_b h_0^{-1}$) (Benjamin and Lighthill 1954; Rottman and Simpson 1989). For $1 < d_b h_0^{-1} < 2$, undulations are formed following the leading bore and the bore is undular in form, with energy dissipation dependent upon vertical wave propagation. These undulations are often observed following the passage of undular bores as an amplitude-ordered packet of solitary waves, known as a soliton. The Morning Glory waves in northeastern Australia are historically the most commonly cited form of such undular bores (Clarke et al. 1981; Smith et al. 1982; Goler and Reeder 2004). For increasing bore strength, however, turbulent motions on the rear side of the bore head become increasingly important for wave-energy dissipation and inhibit the development of solitary waves that may form behind the bore (Rottman and Simpson 1989). Of similar concern is the potential for solitary waves to assist in vertical mixing if the solitary waves propagate behind a turbulent bore (Koch et al. 2008a). Knowledge of each wave packet's evolution is therefore critical to the assessment of both the characteristics of the waves and their potential impacts on the surrounding environment.

Depending on the wave characteristics, bores and solitary waves may generate enough vertical motion to overcome near-surface static stability and generate moist convection. Multiple case studies have shown bores to decrease the stability of the boundary layer and generate vertical motion and turbulent mixing associated with mass convergence on the leading edge of the wave (Karyampudi et al. 1995; Koch and Clark 1999; Coleman and Knupp 2011). The cooling generated by the vertical motion at the leading edge of the bore can lead to cloud formation if the atmospheric moisture content is sufficient. This condensation has been documented to result in the formation of laminar, roll-shaped clouds, termed Morning Glory waves in Australia [e.g., Haase and Smith (1984) and Goler and Reeder (2004)], or even strong to severe convection if the free atmosphere is conditionally unstable (e.g., Karyampudi et al. 1995; Koch and Clark 1999; Locatelli et al. 2002; Watson and Lane 2016).

Because of the complexity of their evolution, bores and solitons pose significant diagnostic and prognostic difficulty. The modifications to the atmospheric profile by bores and solitons and the related potential for moist convection are difficult to quantify unless specific characteristics of the waves are known (Koch and Clark 1999). High-resolution observations of gravity waves are

TABLE 1. Properties of observation systems utilized.

Observing system	Extracted variables	Sampling resolution (min)	Location
Oklahoma Mesonet	T, T_d, w, p, wind speed, wind direction	5	Oklahoma; statewide
ARM surface stations	T, T_d, w, p, wind speed, wind direction	1	North-central OK
Doppler wind lidar	Wind speed, wind direction	2	Norman, OK
AERI	T, w, LWP	2	Norman, OK, and Lamont, OK
NEXRAD radar	Base reflectivity	5	TLX, DDC, VNX, INX, ICT

therefore crucial for accurate analyses of their evolution, influences on their surrounding environment, and their potential to generate moist convection. Recently, the Plains Elevated Convection at Night (PECAN) field campaign utilized a high concentration of mesonet stations and atmospheric profilers to better understand the relationship between bores and nocturnal deep convection (Geerts et al. 2017).

Previous case studies of lower-tropospheric gravity waves have used vertical profiling instruments (e.g., Knupp 2006; Koch et al. 2008a,b; Martin and Johnson 2008); however, many of the previous studies have arguably been limited by a lack of observations that capture both the horizontal and vertical evolution of the waves. The current case is unique due to both the array of instruments available and the waveform observed. We utilize the high spatiotemporal resolution of Oklahoma Mesonet surface observations in concert with vertical profiling observations from two Atmospheric Emitted Radiance Interferometers (AERI) and a Doppler wind lidar (DWL) to provide details on the four-dimensional evolution of a bore-soliton wave complex.

Prior to discussing the wave complex, we provide details of the utilized instruments in section 2. The prewave environment is discussed using both atmospheric profiles and synoptic weather analyses in section 3, and the wave complex is analyzed using observational data and hydraulic theory in section 4. Conclusions and suggestions for future work are provided in section 5. A discussion of how the uncertainty in the vertical profilers impacts the analysis is provided in the appendixes.

2. Overview of instruments

We analyzed the evolution of the lower troposphere prior to, during, and after the gravity wave passage using: 1) the surface meteorological data provided by the Oklahoma Mesonet (Brock et al. 1995; McPherson et al. 2007) and Atmospheric Radiation Measurement stations (ARM; Stokes and Schwartz 1994; Sisterson et al. 2016), and 2) lower-tropospheric profiles provided by the AERI instrument at the ARM site in Lamont, Oklahoma, and the AERI and DWL instruments at the National Weather Center in Norman, Oklahoma. See Table 1 and Fig. 1 for an overview of the observation systems used in this study.

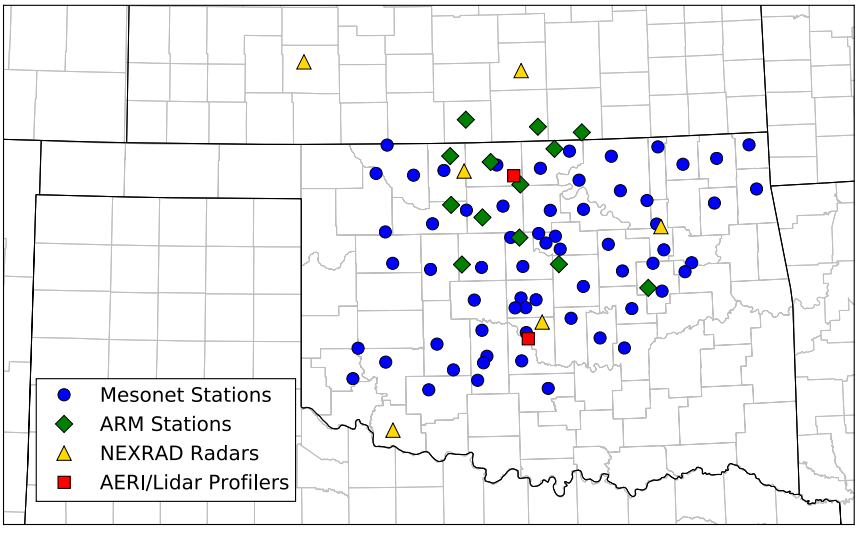

FIG. 1. The observation systems that provided data for this study. Data sources included Oklahoma Mesonet surface stations (5-min sampling; blue circles), ARM surface stations (1-min sampling; green diamonds), AERI/DWL instruments (2-min sampling; red squares), and NEXRAD radars (5-min sampling; yellow triangles).

a. Near-surface observations

Surface observations were primarily available through the Oklahoma Mesonet, a statewide observation network maintained by the Oklahoma Climatological Survey (OCS). The network provides kinematic and thermodynamic surface data at 5-min temporal resolution, with a spatial resolution (~40 km) far surpassing that of nationally distributed surface observation networks. Oklahoma Mesonet data are subjected to rigorous quality-assurance methods that consist of laboratory calibration, on-site intercomparison, and automated and manual quality assurance. While the Oklahoma Mesonet (hereinafter Mesonet) is capable of reporting and archiving 1-min and finer data, only the standard 5-min data were available for use in this study.

The ARM surface stations used in this study are part of the ARM Southern Great Plains (SGP; Sisterson et al. 2016) site in north-central Oklahoma and south-central Kansas. These instruments automatically collect 1-min-averaged surface thermodynamic and kinematic data, which are routinely provided to the Site Data System via high-speed communications. While ARM has several quality assurance procedures, including automatic flagging and manual quality reports, the quality of data for the present study proved to be questionable at times when compared to Mesonet data. In the case of questioned data quality, the Mesonet data were used to adjust ARM data via bias correction.

b. Vertical profiling instruments

1) Atmospheric Emitted Radiance Interferometer

The AERI is a passive infrared interferometer that measures downwelling atmospheric radiance at 1 cm^{-1} resolution between 3.3 and 19.2 μm (Knuteson et al. 2004a). The interferometer samples atmospheric radiance every 2 s, although multiple samples (typically 12 s) are averaged to reduce the random noise. A principal component–based noise filter (Turner et al. 2006) is used to reduce the magnitude of the random error in the observed spectra. Periodic automated calibration using two internal blackbodies results in absolute radiance measurement uncertainties of less than 1% from the ambient radiance (Knuteson et al. 2004b). One of the blackbodies is maintained at a constant temperature of 60°C while the other's temperature is allowed to fluctuate with the ambient atmospheric temperature. The use of a blackbody at ambient temperature ensures that the AERI is calibrated to a temperature resembling atmospheric conditions (Feltz et al. 2003; Knuteson et al. 2004b).

The downwelling infrared radiance (the observation vector) is sensitive to the atmospheric temperature, water vapor, liquid water path, and cloud droplet effective radius (the state vector). An optimal estimation–based retrieval algorithm (AERIoe), developed by Turner and Löhnert (2014), is an iterative Gauss–Newton retrieval technique that uses a forward radiative transfer model to compute an estimate of the observation vector from the state vector. The state vector is then iteratively adjusted until convergence is achieved between the forward calculation and the observation vector. To provide a full error characterization of the retrieved solution, AERIoe propagates uncertainty in the AERI radiance observations, the prior dataset used to constrain the retrieval (which is a climatology of radiosonde profiles from the ARM SGP site), and the forward model.

The AERIoe algorithm uses a synthesis of profiles of temperature and mixing ratio derived from a climatology of radiosondes released from the ARM SGP site to create an a priori probability density function (PDF). This PDF is used to constrain the state vector to stabilize the retrieval process and improve solution derivation efficiency. The retrievals are performed with a statically defined vertical grid, with the resolution ranging from 25 m near the surface to approximately 800 m at 3 km above the surface (Turner and Löhnert 2014).

2) Doppler wind lidar

The DWL located in Norman, Oklahoma, is a Halo Streamline unit, which emits pulses of 1.5-μm wavelength laser energy (Pearson et al. 2009) and captures observations on a consistent gate size of 18 m. The DWL measures the radial velocity by measuring the Doppler shift of the laser's energy in the backscattered return. The primary scatterers at this wavelength are aerosol particles, which are small and can be used as tracers of air motion. This lidar has a three-dimensional scanner, which allows measurements anywhere in the hemisphere above the lidar. An eight point plane-parallel indicator (PPI) scan is performed at a specified elevation angle (e.g., 40° or 70° as in the case of the Norman DWL) every 2 min, from which horizontal wind speed and direction are derived using the velocity–azimuth display (VAD) technique.

While the VAD method is effective at measuring both horizontal wind speed and direction, it inherently introduces error for complex phenomena such as gravity waves. The VAD technique assumes horizontal cross sections of the conical volume sampled during the PPI scan to be homogeneous (Lundquist et al. 2015). However, for phenomena such as gravity waves where inhomogeneities in the kinematic profiles may exist during the PPI scan, the VAD assumption of homogeneity reduces the ability to capture the maxima and minima of the kinematic field.

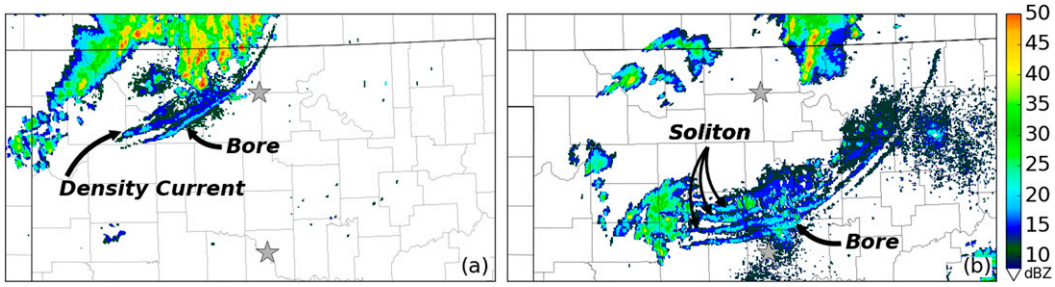

FIG. 2. NEXRAD WSR-88D composite reflectivity data at (a) 0700 and (b) 0920 UTC 10 Aug 2014. Reflectivity values below 8 dBZ were filtered out to emphasize the reflectivity returns of the density current and wave packet. The current and wave features are identifiable by the southwest–northeast-arcing bands in low (generally 8–20 dBZ) reflectivity values. The gray northern and southern stars represent the locations of the ARM SGP (Lamont, OK) and National Weather Center (Norman, OK) locations, respectively.

As such, we only used the PPI scan collected at 70° elevation to reduce the conical volume sampled by the beam and hence the smoothing of the kinematic field.

3. Preevent analysis

On 10 August 2014, wavelike features in northern Oklahoma were visible as fine lines on NEXRAD WSR-88D (Klazura and Imy 1993) displays beginning at approximately 0700 UTC, or 0200 LT (Fig. 2). An outflow boundary originated from a nocturnal mesoscale convective system in south-central Kansas and propagated south-southeastward into north-central Oklahoma. As the outflow boundary entered Oklahoma, another fine line of radar reflectivity—the suspected bore—appeared to gradually separate itself from the outflow boundary and propagate independently (Fig. 2a). Additional fine lines formed behind the leading wave, with the developed wave packet propagating southeastward as an arc throughout Oklahoma during the remainder of the nocturnal hours (Fig. 2b). As will be shown, the outflow boundary and wavelike features took the form of a bore and soliton induced by a convectively generated density current.

a. Synoptic conditions

At 0000 UTC 10 August 2014, a low-amplitude, midlevel short-wave trough translated over the Texas Panhandle and initiated lee cyclogenesis in eastern Colorado and western Kansas. Subsidence in the right-exit region of the associated jet streak induced clear skies over much of Kansas and Oklahoma. The clear skies likely led to strong radiative cooling and the development of a surface-based inversion. By 0600 UTC, the north–south orientation of the low-level trough axis favored a south-southwesterly oriented low-level jet. Persistent warm air advection between 900 and 700 mb (1 mb = 1 hPa) warmed the atmosphere atop the radiatively cooled planetary boundary layer. A maximum in surface equivalent potential temperature existed in north-central Oklahoma. Atmospheric moisture increased from the southwest to the northeast between the surface and 850 mb, while an elevated mixed layer was advected atop this low-level moisture plume (Fig. 3).

By 1200 UTC, the low- to midlevel atmospheric winds veered as the midlevel short-wave trough progressed into east-central Kansas (Fig. 4). Weak, southwesterly near-surface winds advected drier air from the Texas Panhandle eastward into Oklahoma. As midlevel winds veered significantly to a northwesterly direction, downward mixing of momentum and eastward translation of the lee cyclone contributed to veering of the low-level jet.

b. Prebore vertical profiles

A preevent analysis of radiosonde, AERI, and DWL atmospheric profiles suggested the presence of a low-level ducting layer at both Lamont and Norman, Oklahoma, at 0600 UTC (0100 LT). This ducting layer was diagnosed from a rapid increase in Scorer parameter [Eq. (1)] between the surface and 225 m, with a rapid decrease in the Scorer parameter just above this level (Fig. 5). Further, vertical profiles of the Brunt–Väisällä frequency suggested a near-surface inversion was present prior to the passage of the gravity waves (not shown). While the initial generation of waves required the presence of this inversion, the atmospheric stability likely did not directly contribute to the ducting layer. Instead, the contribution of the curvature term to the Scorer parameter was several orders of magnitude greater than the stability term, which suggests that the low-level jet was primarily responsible for the wave-energy ducting (Fig. 5). No critical layer, or layer where the wind component orthogonal to the direction of the bore movement is equivalent to the propagation speed of the bore, was observed in the prebore vertical profiles.

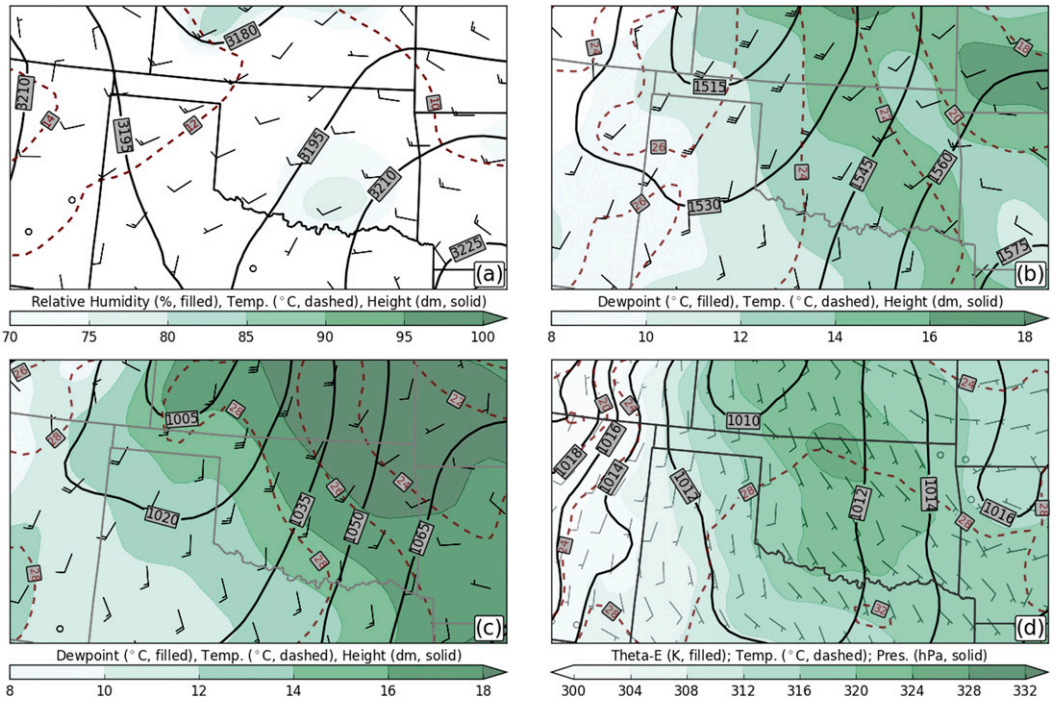

FIG. 3. North American Regional Reanalysis (NARR) data at 0600 UTC 10 Aug 2014 from (a) 700 mb, (b) 850 mb, (c) 900 mb, and (d) 10 m above ground level. The following information is detailed on each plot: isohypses in solid black (alternatively, isobars for near ground); isotherms in dashed red; wind speed shown by barbs in units of m s^{-1}; relative humidity (700 mb), dewpoint (850 and 900 mb), and equivalent potential temperature (near ground) in fill.

4. Event analysis

The influences of the density current and gravity waves on the near-surface atmosphere were deduced using observations from the Oklahoma Mesonet and ARM SGP sites. Determination of the wave type is possible using surface observations alone: the perturbations of near-surface variables may be used to approximate the vertical influences of hydrostatic waves (e.g., through hydraulic theory) (Christie et al. 1979; Koch et al. 1991). Four-dimensional analyses, however, require the inclusion of vertical profiling instruments. The AERI and DWL instruments were therefore essential to the evaluation of the vertical evolution of thermodynamic and kinematic variables and the overall characteristics of the gravity wave complex.

a. Radar, ARM, and Mesonet observations

1) SURFACE DATA COLLECTION

The difference in the temporal resolution of the ARM (1 min) and Mesonet (5 min) observations presented a unique opportunity to compare the ability of 5-min data to that of 1-min data in adequately resolving the finescale meteorological features associated with gravity waves. Aside from the comparative analysis, the Mesonet and ARM surface data were utilized in conjunction with the NEXRAD WSR-88D network to estimate the temporal evolution of the gravity wave complex.

When documenting perturbations in near-surface variables, NEXRAD WSR-88D data were used to determine the time of radar-depicted fine line passage over a site. Only the Mesonet and ARM stations that were passed over by the radar-depicted fine lines of the density current or bore were considered relevant to the study. Data from surface stations influenced by precipitation were discarded from the dataset to limit the inclusion of precipitation-induced perturbations in surface variables.

The presence of waves was diagnosed by observing perturbations in surface pressure p, temperature T, and water vapor mixing ratio w measured at 1.5 m. The base state and postwave values were documented to analyze the magnitude of wave-induced perturbations. As an example, the decomposition of an arbitrary variable X is defined as

$$X = \overline{X} + X', \tag{2}$$

where $\overline{X}$ is the base (i.e., prewave) state of a variable and X' is the perturbation from the base state following

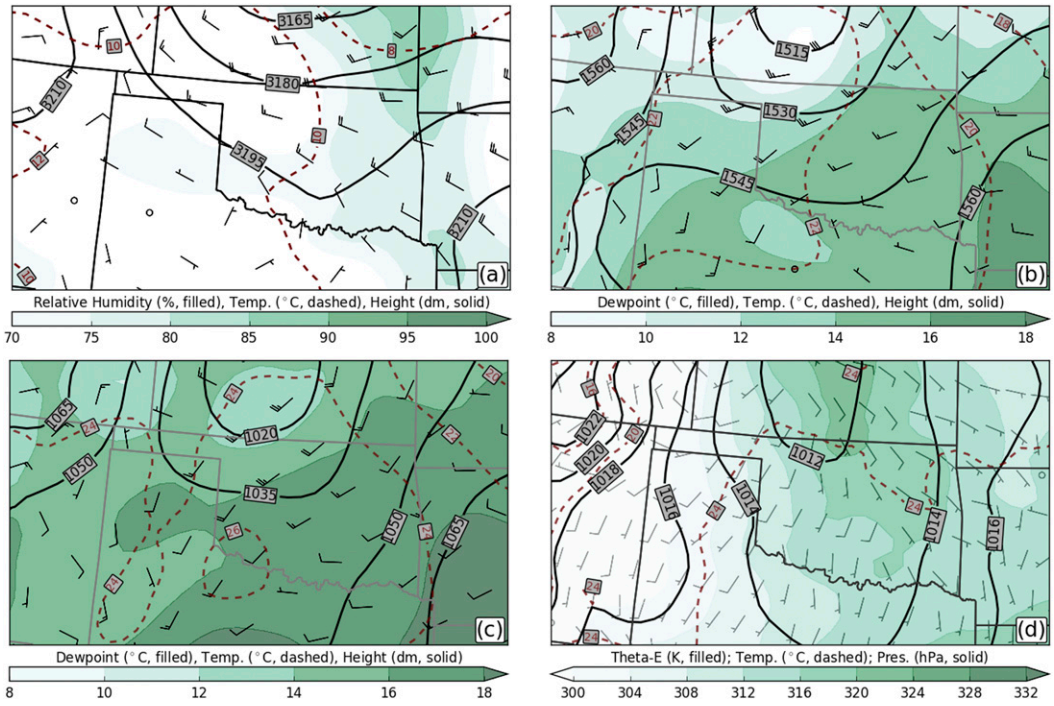

FIG. 4. As in Fig. 3, but at 1200 UTC 10 Aug 2014.

wave passage. A density current was identified by an observed positive perturbation in pressure with a subsequent negative perturbation in temperature and/or mixing ratio, while bore passage was identified via positive perturbations in both surface pressure and temperature [signatures identified in previous literature, e.g., by Koch et al. (1991)]. While density currents may induce a positive perturbation in mixing ratio under certain conditions, in this case the density current was characterized by negative perturbations from the prewave state.

2) SURFACE DATA ANALYSIS

(i) Spatial analysis

Perturbations associated with the density current or bore passage were converted into tendencies by dividing the perturbation magnitude by the perturbation duration, yielding time derivatives of pressure p, temperature T, and mixing ratio w. The perturbation duration was defined as the time elapsed between the initial deviation from the prewave state and the succeeding point of maximum curvature in the time series, which typically corresponded to the maximum perturbation. Pressure and temperature tendencies associated with the passage of the density current and gravity waves were plotted for all relevant surface stations to visualize the spatiotemporal evolution of both features (Figs. 6 and 7), where the 5-min Mesonet data are denoted as empty circles and 1-min ARM data are denoted as hatched circles.

Large, negative temperature tendencies (blue) in northern Oklahoma defined the peak strength of the density current, which weakened in magnitude as it propagated to the southeast and became diffuse. The bore was evident in both the ARM and Mesonet surface data, with positive temperature tendencies (red) decreasing in magnitude as the bore propagated southeast (Fig. 6). Both bore- (brown) and density current–induced (blue) pressure tendencies (Fig. 7) were approximately proportional to the temperature tendencies observed at the same station (Fig. 6). This agreement should be expected, given that stronger bores tend to have more significant turbulence in the following wake and thus may mix a larger quantity of potentially warmer air toward the surface (Rottman and Simpson 1989; Koch et al. 2008a). The magnitudes of the pressure and temperature tendencies were also spatially correlated, decreasing in value as the bore and density current progressed southeastward.

The temperature and pressure perturbations for both the density current and bore are marginally correlated (correlations of −0.41 and 0.38, respectively; both significant beyond the 95th percentile) (Fig. 8a). While there appears to be no definitive theory proposed by previous literature explaining these correlations, we speculate on this topic in the discussion and conclusions

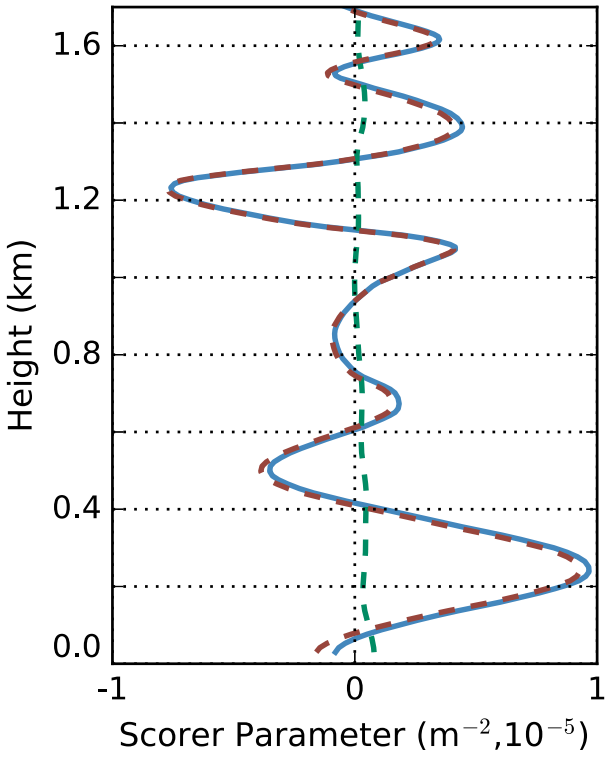

FIG. 5. Radiosonde-derived vertical profiles of the Scorer parameter (solid blue), and individual curvature (dashed red) and stability (dashed green) terms. The radiosonde was launched at 0533 UTC at Lamont, approximately 2 h before gravity wave passage.

section of the paper (section 5). A statistically significant correlation (−0.61) also existed between the magnitudes of mixing ratio and pressure tendencies for the density current; however, no significant correlation between these two variables exists for the bore (Fig. 8b). The reason for the lack of correlation between the mixing ratio and pressure tendencies for the bore is unclear, although this lack of correlation may be case specific based on the inconsistent results presented by previous literature [e.g., sustained perturbations in mixing ratio that are positive, as in this study (Fig. 9c); negative in the case of Hartung et al. (2010); or a more complex combination of negative and positive perturbations shown in Koch et al. (2008a)].

The qualitative similarities between the 1- and 5-min data demonstrate the effectiveness of the lower-resolution observations in diagnosing the presence of atmospheric bores, as the temperature tendencies derived from the 1-min (ARM) and 5-min (Mesonet) data are similar in magnitude. However, the relatively higher values in ARM-derived pressure tendencies suggest that the 5-min data do not always accurately depict the quantitative characteristics of the bore. We believe this to be the result of pressure perturbations occurring more rapidly than temperature perturbations in this case, which may have led to a greater chance of pressure perturbations not being resolved by the lower-resolution data.

(ii) Time series analysis

The time series of thermodynamic perturbations (i.e., p, T, and w) were defined as deviations from the observed prewave base state [Eq. (2)]. The perturbation time series from three Mesonet stations extending along the path of the wave complex were compared to the closest ARM station to analyze the importance of temporal resolution (Fig. 9). The Mesonet and ARM

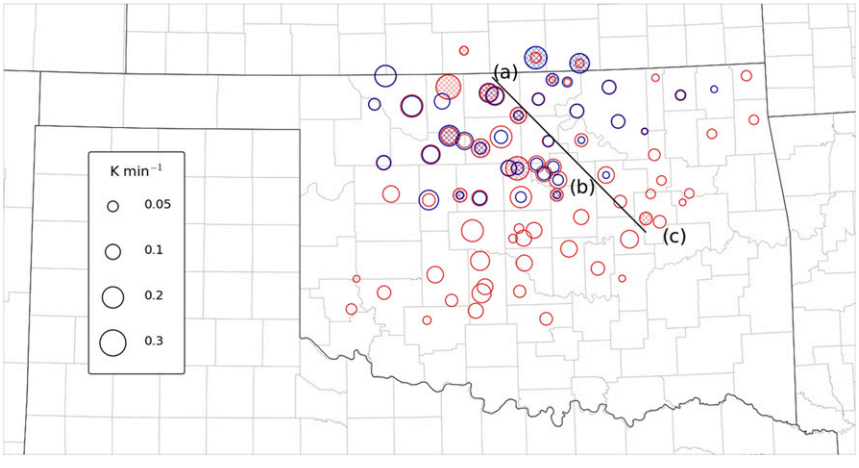

FIG. 6. Temperature tendency ($\partial T \partial t^{-1}$) induced by the density current (<0, blue) and bore (>0, red), as observed by 1-min ARM (hatched) and 5-min Oklahoma Mesonet (hollow) surface stations. Locations a, b, and c on the black line correspond to Mesonet stations used for the similarly labeled perturbation meteograms in Fig. 9.

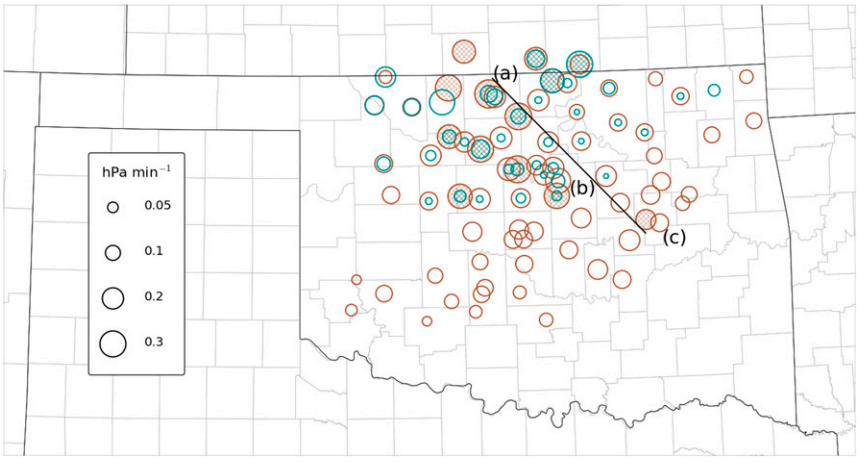

FIG. 7. As in Fig. 6, but for pressure tendency (>0, $\partial p \partial t^{-1}$) induced by the density current (blue) and the bore (brown).

stations were each approximately 10 km apart, which may have introduced a source of error into the analysis, although Figs. 6 and 7 suggest the bore had fairly consistent characteristics over such a distance.

At the northwesternmost station (Medford, Oklahoma; Fig. 9a), the bore was identified by pronounced positive perturbations in pressure and temperature beginning at ~0655 UTC. A density current signature followed immediately thereafter, in this case signified by a positive pressure perturbation coincident with a decrease in temperature and mixing ratio. Based on the ARM data, multiple oscillations in surface pressure occurred after the passage of the density current, suggesting additional waves existed atop the current. Previous literature has found waves propagating atop density currents to be of either Kelvin–Helmholtz (e.g., Droegemeier and Wilhelmson 1987; Nasr-Azadani and Meiburg 2015) or solitary wave type (e.g., Koch et al. 1991), although no kinematic profiles were available near the Medford site and thus the nature of these waves cannot be investigated at this location.

Pressure and temperature signatures observed at the second station at ~0830 UTC (Perkins, Oklahoma; Fig. 9b) are indicative of a leading bore and a trailing soliton (i.e., an undular bore). The oscillations in 1-min surface pressure following the bore passage and prior to the density current passage suggest the presence of solitary waves, although no near-surface perturbations in mixing ratio and temperature were evident. In contrast to the Medford data, no additional waves were evident at Perkins following the passage of the density current. Observations at Okmulgee, Oklahoma (Fig. 9c), showed smaller perturbations in the 1-min data in comparison to stations a and b, which suggests that the gravity wave complex weakened as it propagated southeast. The lack of perturbations in near-surface mixing ratio and temperature associated with the solitary waves suggests that they were either elevated and did not directly influence the near-surface environment or that the boundary layer was well mixed (i.e., the mixing ratio and potential temperature were vertically constant). No density current signature was observed at Okmulgee. Further, based on the lack of sustained modifications in the near-surface pressure and temperature southeast of Okmulgee (Figs. 6 and 7), the leading wave lost its bore characteristics when solar insolation began destabilizing the surface after sunrise at ~1140 UTC. While pressure perturbations still occurred southeast of Okmulgee (not shown), no surface temperature

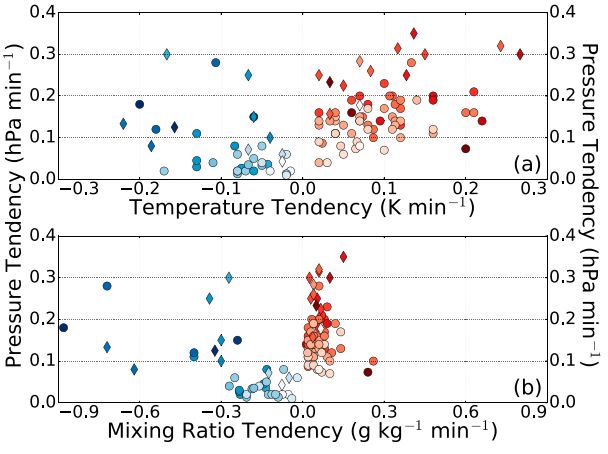

FIG. 8. Pressure tendency ($\partial p \partial t^{-1}$) vs (a) temperature tendency ($\partial T \partial t^{-1}$) and (b) mixing ratio tendency ($\partial w \partial t^{-1}$) associated with the density current (blue) and bore (red), as observed by both ARM (diamonds) and Mesonet (circles) surface stations. The gradient in color saturation corresponds to increasing UTC time, from early (saturated fill) to late (white fill) in the event.

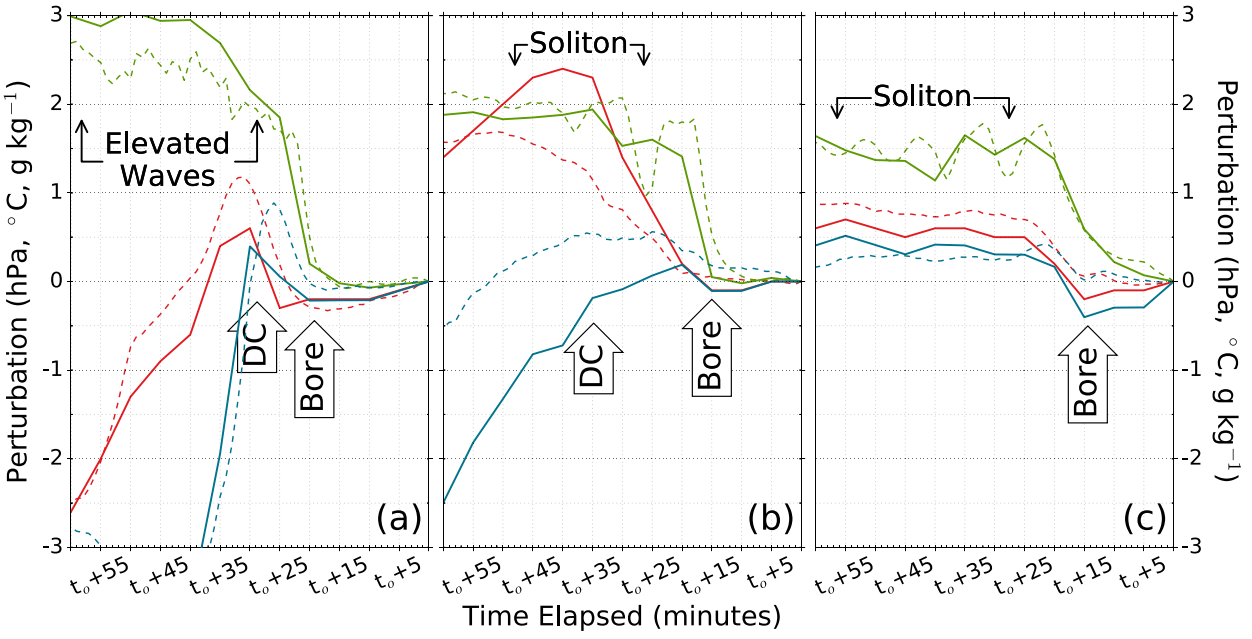

FIG. 9. Time series of density current–induced and/or bore-induced perturbations from the prewave base state (defined as time t_0) of pressure (hPa, green), temperature (K, red), and mixing ratio (g kg^{-1}, blue) at neighboring ARM (dashed) and Mesonet (solid) stations in (a) Medford, OK (t_0 = 0635 UTC), (b) Perkins, OK (t_0 = 0815 UTC), and (c) Okmulgee, OK (t_0 = 0955 UTC). Refer to Fig. 6 or 7 for locations of the Mesonet and ARM stations. The white arrows denote the time of passage of the bore ("bore") and density current ("DC"). Data presented in the reference frame of the bore (i.e., time increases from right to left).

perturbations occurred, which suggests the leading wave was no longer a bore.

Based on the disparities between the 1- and 5-min data in Fig. 9, it is apparent that the 5-min data do not accurately depict the perturbations caused by the bore and trailing soliton. In fact, the 5-min data do not capture any solitary waves following the passage of the bore at Perkins, whereas the 1-min data suggest the presence of at least one solitary wave (Fig. 9b). This deficiency is likely due to the inability of the 5-min data to resolve the solitary wave, which has a period of approximately 10 min. The 5-min averaging window of Mesonet data would therefore dilute the solitary wave signature and limit the ability to infer the presence of any solitary waves. We suggest a required minimum of four data points per wave passage to ensure that the presence of each wave could be deduced by capturing extrema in p, T, and w—this would require a sampling resolution of 2.5 min in this case.

b. *AERI and lidar observations*

1) LAMONT, OKLAHOMA

At the ARM central facility near Lamont, an AERI was used as the primary source of vertical profiling information. A DWL was not available at the Lamont facility, so vertical profiles of the Scorer parameter could not be derived. However, vertical profiles of thermodynamic variables still provided sufficient information for analyzing the time–height cross-sectional characteristics of the bore and density current.

(i) Prewave

While the water vapor mixing ratio within the nocturnal boundary layer progressively increased prior to bore passage, the free atmosphere relative humidity was at or below 50%. Additionally, a surfaced-based inversion had developed in response to radiative cooling, which thereby marked an increase in near-surface stability. The inversion was not as strong as in other strong bore cases (e.g., Karyampudi et al. 1995; Koch et al. 2008a; Hartung et al. 2010), but this apparently was not a significantly limiting factor given the eventual development of a gravity wave packet. Because of the lack of DWL at the Lamont location, it is relatively uncertain whether a favorable ducting layer existed atop the nocturnal boundary layer at this time in the bore life span. Based on the synoptic analysis, however, a favorably oriented low-level jet existed and likely contributed to the development of such a ducting layer (Fig. 3).

(ii) During and postwave

Bore-related influences at Lamont were first observed at approximately 0720 UTC (0220 LT) with the density

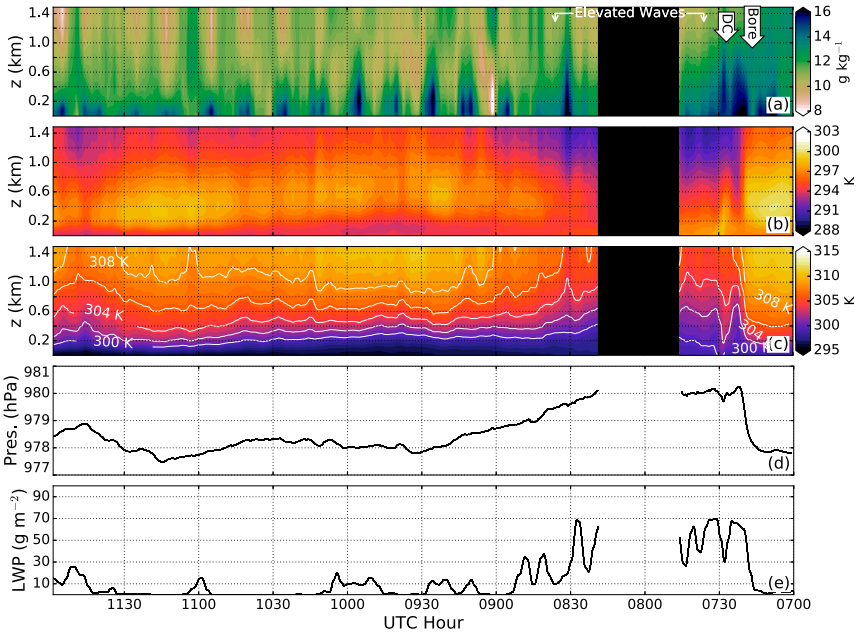

FIG. 10. Thermodynamic variables retrieved from the AERI near Lamont, OK, between 0700 and 1200 UTC. (a) Time–height cross section of mixing ratio (g kg^{-1}), (b) time–height cross section of temperature (K), (c) time–height cross section of potential temperature (K) with select adiabats delineated with white contours, (d) AERI-level pressure (hPa) at approximately 30 m AGL, and (e) liquid water path (g m^{-2}). Periods when the AERI hatch was closed due to rainfall are denoted by a black bar. Pressure values were calculated via the hypsometric equation using state vector data from the AERI. The white arrows denote the time of passage of the bore ("bore") and density current ("DC"), while the white bracket denotes the period of elevated wave influence. Data are presented in the reference frame of the bore (i.e., time increases from right to left).

current passage at 0730 UTC (Fig. 10). At heights above 0.2 km, rapid negative temperature perturbations occurred on the front side of the bore head, while positive pressure perturbations occurred from 0.2 to 1.5 km above the surface (Fig. 11). The presence of the bore was identified by negative temperature perturbations aloft occurring simultaneously with a vertical lifting of the potential temperature profile, suggesting this cooling was the result of layer lifting rather than cold air advection. Thereafter, the density current passed over Lamont, and the thermodynamic influences of the bore were no longer evident.

Based on the brevity of the postbore surface warming event between 0725 and 0730 UTC, it appears the rear side of the bore head coincided with the front of the density current, which limited the typical bore-induced downward mixing of potentially warmer air. However, a brief, rapid increase in low-level temperature was observed at ~0730 UTC that resulted from subsiding potentially warmer air on the rear side of the bore head collocated with compressional warming in advance of the density current [a phenomenon similarly observed with cold fronts, e.g., Hartung et al. (2010)]. Shortly thereafter, negative temperature perturbations were observed within the entire 0–1.5-km column, with progressive cooling of the near-surface layer between ~0730 and 0930 UTC likely caused by cold air advection within the density current (Figs. 10b,c and 11). It is interesting to note that the shape of the density current appears to be identifiable by the positive pressure perturbations in the time–height cross section (Fig. 11a), as this period also coincided with the occurrence of low-level temperature advection.

Multiple elevated waves appear to have propagated atop the density current, visible via oscillations in liquid water path (LWP) and the adiabats within the 0.4–1.5-km layer (Figs. 10a,c). Immediately following the passage of these elevated waves (~0830 UTC), the temperature profile and surface pressure began to return to their base state (Fig. 11), suggesting these elevated waves were either gravity waves or generated by Kelvin–Helmholtz instability. We further suggest that the quasi-permanent increase in surface pressure at this location (between ~0720 and 0830 UTC) was caused by near-surface cold air advection associated with the density current, rather than the result of an undular bore.

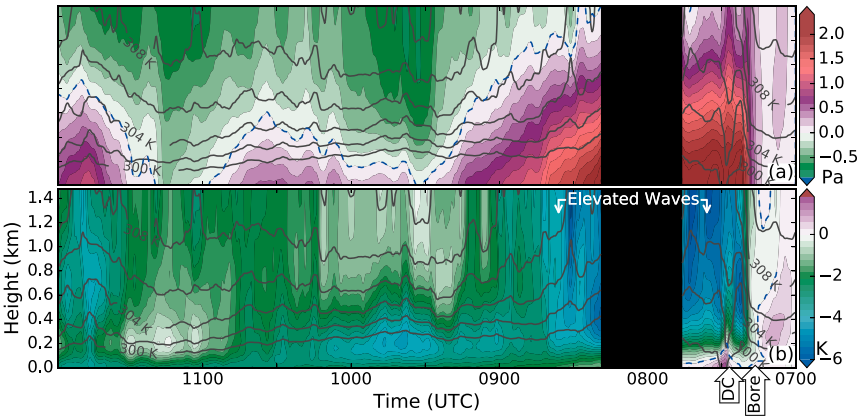

FIG. 11. Perturbations of (a) pressure (Pa) and (b) temperature (K) from the pre–gravity wave base state, defined as 0700 UTC, derived from data from the Lamont, OK, AERI. Pressure values were calculated via the hypsometric equation using state vector data from the AERI. The dashed blue line denotes instances in individual vertical profiles with zero deviation from the base-state values. Adiabats are plotted at intervals of 2 K. Periods when the AERI hatch was closed due to rainfall are denoted by a black bar. The white arrows denote the time of passage of the bore ("bore") and density current ("DC"), while the white bracket denotes the period of elevated wave influence. Data are presented in the reference frame of the bore (i.e., time increases from right to left).

2) NORMAN, OKLAHOMA

(i) Prewave

The bore arrived at Norman approximately 2.5 h after arriving at Lamont, which extended the period of radiative cooling and increased the associated strength of the surface-based inversion. Vertical kinematic profiles derived from the DWL in Norman (Fig. 12) suggested that by the time the bore arrived at Norman, the low-level jet had strengthened in comparison to the 0600 UTC synoptic analysis (Fig. 4). This strengthening of the low-level jet likely enhanced the shear-induced ducting layer located atop the nocturnal boundary layer, especially given the calm winds near the surface (data not shown). The nocturnal boundary layer had become nearly saturated prior to bore passage, but was overlaid by significantly drier air, similar to Lamont. We suggest this drier air likely contributed to the limited longevity of moist convection in comparison to locations in eastern Oklahoma (sparse convection shown in Fig. 2).

(ii) During and postwave

As depicted in Figs. 6 and 7, the density current had become diffuse by the time it propagated into central Oklahoma. Following the initial wave passage over Norman at ~0950 UTC (0450 LT), profiles of the horizontal wind components (Figs. 12a–c), mixing ratio (Fig. 13a), and temperature (Figs. 13b,c) show sustained modifications to the near-surface environment, suggestive of a bore passage. Specifically, the presence of a bore is evidenced by sustained positive perturbations of near-surface temperature and pressure from the prewave environment and the rotation of the near-surface winds toward the direction of the wave movement following the passage of the wave (Figs. 12–14).

Oscillations in both the kinematic and thermodynamic variables persisted following the bore passage (Figs. 12 and 13). The near-surface potential temperature profile at Norman was not disturbed by these oscillations, and given that the boundary layer was not well mixed as indicated by the presence of a vertical gradient in potential temperature, this lack of disturbance suggests that the postbore waves did not extend to the surface (Fig. 14). We further conclude these waves could not have originated from Kelvin–Helmholtz instabilities, given that the gradient Richardson number (not shown) was greater than the critical threshold for Kelvin–Helmholtz wave formation of 0.25 (Fritts and Rastogi 1985). These factors suggest that an elevated soliton was present. However, the waveform of the soliton deviated from the amplitude ordering of typical undular bores: it is apparent that the solitary waves were not amplitude ordered, and the amplitude of the waves increased from the first to the fourth solitary waves, thereafter decreasing with each subsequent wave.

Based on the derived Scorer parameter cross sections (Fig. 15), a prominent wave duct existed with a height between 0.4 and 0.5 km above the surface prior to the bore passage. It appears that a second persistent ducting layer existed within an elevated shearing layer following

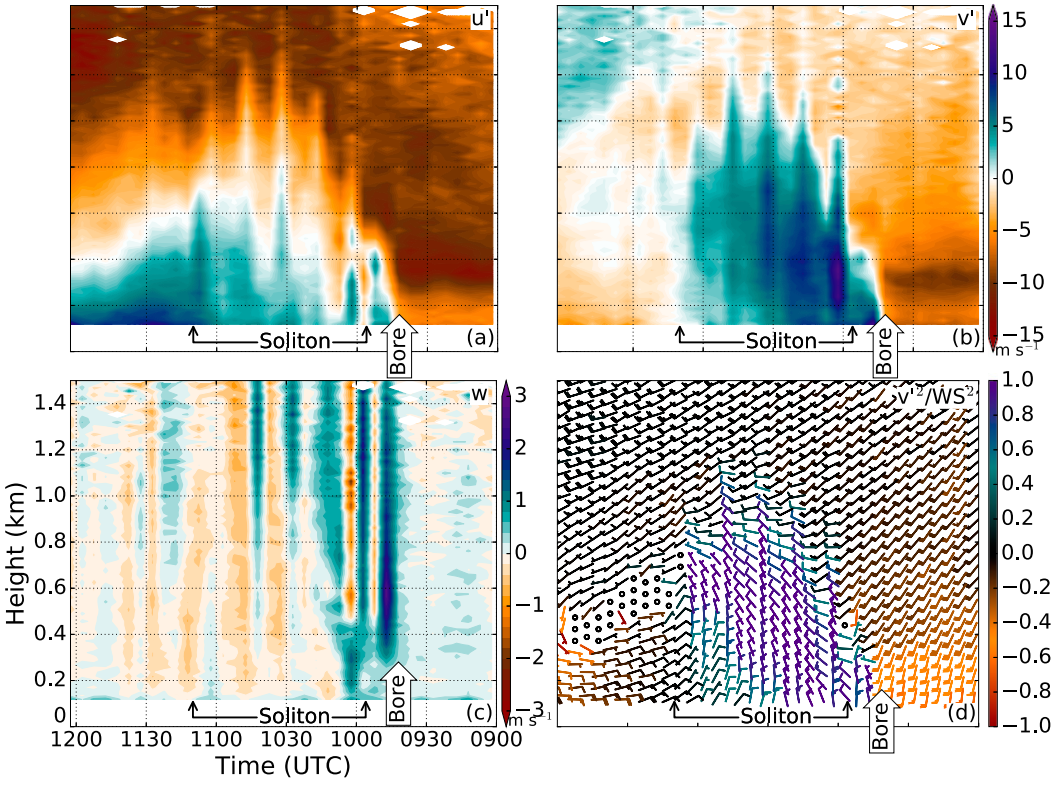

FIG. 12. Vertical kinematic profiles derived from the Norman, OK, DWL of (a) bore-tangential wind speed, (b) bore-orthogonal wind speed, (c) vertical motion, and (d) fractional component of the wind in the direction of bore propagation. The coordinate system was transformed with the positive *y* axis oriented toward the direction of bore movement when passing over Norman (the bore was moving toward the south-southeast at approximately 150° from true north). The white arrow denotes the time of bore passage ("bore"), while the black brackets denote the period of soliton influence. Data are presented in the reference frame of the bore (i.e., time increases from right to left).

the bore passage. The center of the elevated ducting layer resided approximately 1.0 km above the surface and is visible via the vertical shearing of the bore-orthogonal wind component (Fig. 12) atop the layer of sustained bore influence (i.e., the layer below ~0.8–1.0 km AGL). This postbore ducting layer is likely not a violation of the linear assumptions necessary to derive the Scorer parameter. Rather, the postbore environment may be considered as a new base state, wherein the flow is mostly independent of the perturbations. This ducting layer, primarily induced by the curvature of the wind, was therefore likely generated by the development of an elevated inversion following the passage of the bore. The atmosphere below the elevated inversion would have been modified by the bore, whereas the free atmosphere above the inversion would have maintained its prebore characteristics. The resultant enhanced wind shearing is evident in both the kinematic and Scorer parameter profiles (Figs. 12 and 15). The background large-scale subsidence, as discussed in section 3a, likely led to the gradual descent of this postbore elevated ducting layer.

The solitary waves propagated within the elevated inversion, which we suggest was generated by the passage of the bore. Under the assumption that the vertical motion associated with the bore was adiabatic, layers vertically displaced by the bore may be identified by the vertical redistribution of potential temperature. In particular, the vertical displacement of adiabats visible in Fig. 14 suggests that the near-surface inversion was vertically displaced by the bore. Contraction of the adiabats between 0.5 and 1.0 km suggests that the inversion was predominantly relocated to this layer of the atmosphere. Further, Karyampudi et al. (1995) and Koch and Clark (1999) found that the vertical displacement induced by bores varies according to an approximately parabolic function. This would lead to a relative compression of adiabats above the height of maximum vertical displacement, which would further contribute to the development of an elevated inversion. We therefore suggest that the elevated inversion formed via the combination of the following: 1) the vertical displacement of the original surface inversion, and 2) the

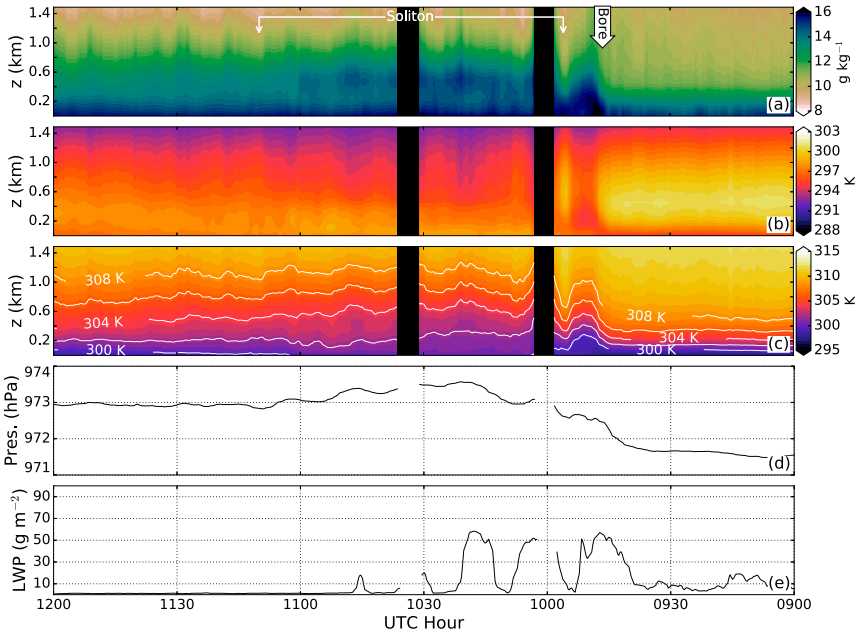

FIG. 13. As in Fig. 10, but for the Norman, OK, AERI between 0900 and 1200 UTC. Black bars denote time periods when AERI observations were significantly attenuated. The white arrow denotes the time of bore passage (''bore''), while the white bracket denotes the period of soliton influence.

relative compression of adiabats above the height of maximum bore-induced ascent.

While a potential third ducting layer was periodically observed near the surface following bore passage (0.1–0.3 km; 1000–1100 UTC), oscillations in the strength of this feature appear to coincide with the kinematic oscillations induced by the solitary waves (Figs. 12c and 14). As such, we believe that this feature was caused by the circulation within the waves themselves, and therefore would not have contributed to the ducting of the wave. The lack of a persistent ducting layer below the waves therefore provided a pathway for wave-energy dissipation.

c. *Hydraulic theory considerations*

In a stratified atmosphere, a density current may generate a hydraulic jump, which may take the form of an atmospheric bore. Hence, hydraulic theory is applicable

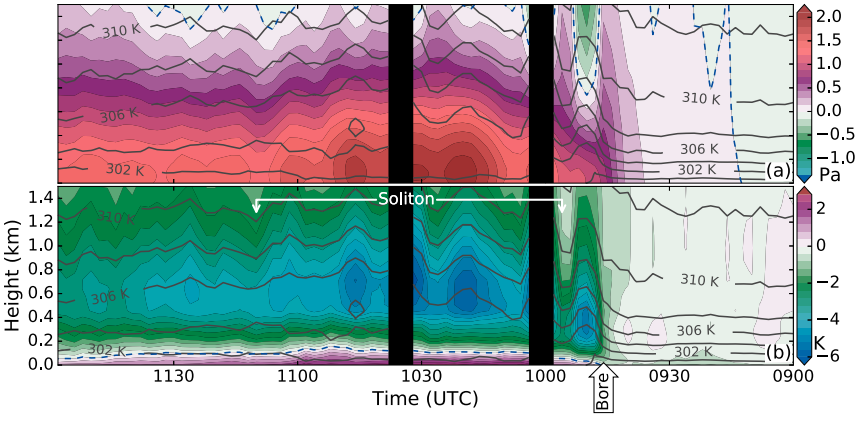

FIG. 14. As in Fig. 11, but for the Norman, OK, AERI between 0900 and 1200 UTC. The pre–gravity wave base state was defined as 0900 UTC. Black bars denote time periods when AERI observations were significantly attenuated. The white arrow denotes the time of bore passage (''bore''), while the white bracket denotes the period of soliton influence.

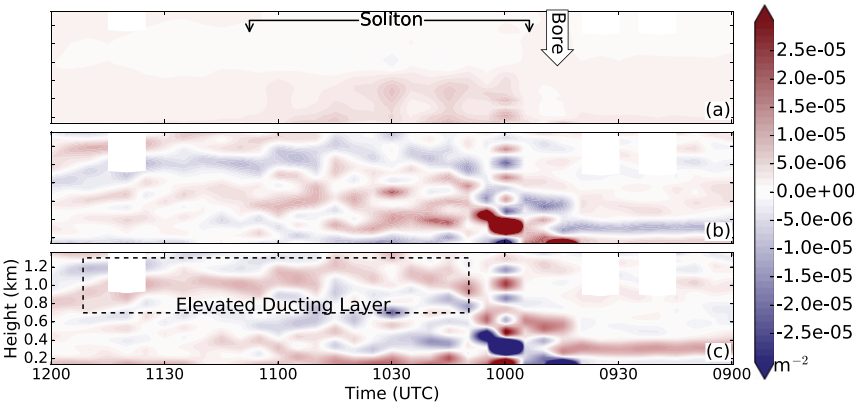

FIG. 15. Temporal cross sections derived from the Norman, OK, AERI and DWL observations of the individual (a) stability and (b) curvature terms of the (c) Scorer parameter. Positive values are shaded red, while negative values are shaded blue. The white arrow denotes the time of bore passage ("bore"), the bracket denotes the period of soliton influence, and the dashed rectangle denotes the elevated ducting layer. Data are presented in the reference frame of the bore (i.e., time increases from right to left).

to bores and may be used to help validate observationally derived conclusions; detailed discussions of the derivations of hydraulic theory may be found in Rottman and Simpson (1989), Koch et al. (1991), Koch and Clark (1999), and Koch et al. (2008a). The presented form of hydraulic theory, originally derived by Rottman and Simpson (1989), considers only cases of gravity waves being bound from above by a ducting layer and below by a solid ground interface. The presented theory is therefore not applicable to the elevated soliton, and was applied only to the density current and bore in northern Oklahoma where the bore had recently propagated ahead of the density current. Furthermore, the application of hydraulic theory to observed bores should be strictly applied in a qualitative sense only, owing to complexities arising from the neglect of mixing, turbulence, wind shear, moisture, leakage of wave energy, and any nonhydrostatic effects. As a source of validation for the usage of hydraulic theory for this case, we compared the theoretically derived quantitative results to those derived from observations.

Rottman and Simpson (1989) defined the strength of the bore to be a function of two nondimensional parameters: 1) the Froude number (Fr) and 2) the ratio of the depth of the density current to the depth of the inversion layer:

$$\mathrm{Fr} = \frac{U - C_{\mathrm{dc}}}{C_{\mathrm{gw}}} = \frac{U - C_{\mathrm{dc}}}{(g' h_0)^{1/2}} = \frac{U - C_{\mathrm{dc}}}{(g h_0 \Delta\theta \theta_{\mathrm{vw}}^{-1})^{1/2}} \quad \text{and} \quad (3)$$

$$D_0 = \frac{d_{\mathrm{dc}}}{h_0}. \quad (4)$$

In this case, C_{dc} is the observed density current propagation speed, C_{gw} is the propagation speed of a hydrostatic wave, N is the Brunt–Väisälä frequency, h_0 is the precurrent inversion layer depth, d_{dc} is the depth of the density current measured behind the head of the current, and θ_{vw} is the virtual potential temperature on the warm side of the density current. The density current depth d_{dc}, density current propagation speed C_{dc}, and gravity wave propagation speed C_{gw} may be calculated using expressions dependent only upon physical variables (Rottman and Simpson 1989; Koch et al. 1991, 2008a):

$$d_{\mathrm{dc}} = \frac{\theta_{\mathrm{vc}} \Delta p}{\rho_w g[(\rho_c \rho_w^{-1})\theta_{\mathrm{vw}} - \theta_{\mathrm{vc}}]} = \left(\frac{C_{\mathrm{dc}}}{\mathrm{Fr}}\right)^2 \left(\frac{\theta_v}{g\Delta\theta_v}\right), \quad (5)$$

$$C_{\mathrm{dc}} = \mathrm{Fr}\left(\frac{\Delta p}{\rho_w}\right)^{1/2} \approx \mathrm{Fr}\left(g d_{\mathrm{dc}} \frac{\Delta\theta_v}{\theta_v}\right)^{1/2}, \quad \text{and} \quad (6)$$

$$C_{\mathrm{gw}} = \left(g h_0 \frac{\Delta\theta_v}{\theta_v}\right)^{1/2}. \quad (7)$$

Multiple forms of the relationships derived by Koch et al. (1991) have been provided for thoroughness, although the first forms of Eqs. (5) and (6) were used for the calculations of d_{dc} and C_{dc}, respectively. Here, Δp is the hydrostatic portion of the bore-induced pressure increase, the $w(c)$ subscript defines variables on the warm (cold) side of the density current, and $\Delta\theta_v$ is the change in virtual potential temperature across the surface-based inversion ahead of the bore. Additionally, bore depth and bore propagation speed may be calculated using the following equations (Rottman and Simpson 1989; Koch et al. 1991; Koch and Clark 1999):

TABLE 2. Physical variables used for Lamont, Oklahoma, hydraulic theory calculations.

Variable	Value (units)	Descriptor	Data source; calculation method
		Density current related	
h_0	400 (m)	Initial inversion depth	AERI data and 0600 UTC LMN radiosonde
θ_{vw}	306.5 (K)	Virtual θ on warm side of density current	Mesonet surface observations; calculated
θ_{vc}	300.0 (K)	Virtual θ on cold side of density current	Mesonet surface observations; calculated
Δp	3 (hPa)	Change in pressure across density current	Mesonet station raw pressure data
$\overline{u}_1$	3.3 ($m\,s^{-1}$)	Stable layer current orthogonal wind speed	Mesonet; 0600 UTC LMN radiosonde
C_{dc}	21.1 ($m\,s^{-1}$)	Density current propagation speed	Visual estimation from radar
d_{dc}	1050 (m)	Density current depth	AERI data; p', T', w cross sections
		Gravity wave related	
$\overline{\theta_v}$	304 (K)	Avg prebore virtual θ	AERI data; θ, w cross sections
$\Delta\theta_v$	8.16 (K)	Change in virtual θ across inversion	AERI data; θ, w cross sections
H	14 100 (m)	Tropopause depth	0600 UTC LMN radiosonde
C_b	22.0 ($m\,s^{-1}$)	Bore propagation speed	Visual estimation from radar
d_b	1200 (m)	Bore depth	AERI data; p', T', w cross sections
λ_b	11 730 (m)	Bore wavelength	AERI; Periodicity multiplied by C_b

$$C_b = C_{gw}\left[\left(\frac{d_b}{2h_0}\right)\left(1+\frac{d_b}{h_0}\right)\right]^{1/2}, \quad \text{and} \tag{8}$$

$$d_b = \frac{g\Delta\theta\overline{\theta}_v^{-1}d_b(d_b+h_0)(2Hh_0-d_b^2-d_bh_0)}{4h_0^2H}. \tag{9}$$

The variable values input into Eqs. (3)–(9) are provided in Table 2, and the calculated bore and density current characteristics are listed in Table 3.

Of primary consideration is the ability for the developed bore to propagate ahead of the density current. Haase and Smith (1989) determined this separation to depend on the μ parameter, defined as the ratio of the idealized gravity wave propagation speed to that of the density current (i.e., $C_{gw}C_{dc}^{-1}$). The μ parameter in northern Oklahoma, 0.5, was less than that established by Haase and Smith (1989) as the minimum value required for the bore to separate from the density current (0.7), indicating that any developed gravity waves would likely not have separated from the density current. The idea that the gravity waves did not immediately separate from the density current is supported by the following: 1) surface meteogram observations, which show the density current resided nearly immediately behind the bore (Fig. 9a); and 2) the observed and theoretically calculated density current and bore propagation speeds, which suggest that the bore was only propagating slightly faster than the density current. The density current began to dissipate as it propagated toward central Oklahoma, allowing the bore to separate from the current (Figs. 6, 7, and 9b,c).

The magnitude of turbulence behind the bore head is important given its role in dissipating energy rearward from the bore. Koch et al. (2008a) showed that for an undular bore, the intensity of turbulent mixing is strongest ahead of the bore, directly behind the bore head, and beneath the solitary waves. Intense turbulent motion following the bore head has been suggested to lead to the destruction, or limited development, of gravity waves behind the bore (Rottman and Simpson 1989). Rottman and Simpson (1989) defined the magnitude of this turbulence to depend on the strength of the bore [i.e., the ratio of the depth of the bore to the depth of the original

TABLE 3. Calculated variables for Lamont, Oklahoma, hydraulic theory calculations.

Variable	Value (units)	Descriptor	Data source; calculation method
		Density current related	
d_{dc}	1220 (m)	Density current depth	Eq. (5); Physical variables derived from AERI
C_{dc}	23.7 ($m\,s^{-1}$)	Density current propagation speed	Eq. (6); Physical variables derived from AERI
$d_{dc}h_0^{-1}$	2.90 (unitless)	Density current strength	Simple ratio; h_0 observed value as stated in Table 2
$C_{dc}C_{gw}^{-1}$	2.25 (unitless)	Froude number	Simple ratio
		Gravity wave related	
C_{gw}	10.5 ($m\,s^{-1}$)	Idealized gravity wave propagation speed	Eq. (7); physical variables derived from AERI
C_b	24.9 ($m\,s^{-1}$)	Bore propagation speed	Eq. (8); physical variables derived from AERI
d_b	1210 (m)	Bore depth	Eq. (9); iterative solution
$d_bh_0^{-1}$	2.89 (unitless)	Bore strength	Simple ratio; h_0 observed value as stated in Table 2

near-surface inversion ($d_b h_0^{-1}$)] with the following relationship:

$$\begin{cases} \text{Smooth; Undular} & 1 < \dfrac{d_b}{h_0} < 2 \\ \text{Slightly turbulent; Undular} & 2 < \dfrac{d_b}{h_0} < 4 \\ \text{Turbulent; Singular wave} & 4 < \dfrac{d_b}{h_0} \end{cases}.$$

The strength of the bore, estimated to be approximately 3.0 in Lamont and 2.8 in Norman (Norman physical variables not shown; $h_0 \approx 430$ m, $d_b \approx 1200$ m), is indicative of moderate bore-head turbulence. Although turbulence behind the bore head is difficult to identify within the Lamont data because of the close proximity of the density current to the bore, vertical kinematic profiles derived from the DWL in Norman depict turbulent flow following the bore passage based on the rapid vertical fluctuations in the curvature term of the Scorer parameter (0950–1010 UTC; Fig. 15). We suggest that the interaction of this bore-head turbulence with the primary solitary wave may have led to the abnormal increase in vertical velocity magnitude from the bore to the primary solitary wave (Fig. 12c).

Estimates provided by hydraulic theory agree with the observational values well. The fractional relative differences between the calculated and observed values are as follows: density current propagation speed C_{dc} is 0.12, density current depth d_{dc} is 0.16, bore propagation speed C_b is 0.13, and bore depth d_b is 0.01. As suggested by Rottman and Simpson (1989), the positive bias of the calculated bore propagation speed may be due to the overestimation of the hydrostatic pressure increase caused by the passage of the bore within the form of the hydraulic theory equations used here. The positive biases of the other calculated values may also have originated from assumptions made by the theory—namely, the neglecting of atmospheric wind shear and turbulent motion—although a specific cause for the deviations is not known.

As an aside, the observationally deduced depths of the bore and density current were subjectively determined based on perturbations in the vertical profiles of temperature (Figs. 10 and 11). This subjectivity may have introduced errors in the depth estimates derived from observations. However, the observationally derived estimates of the bore and density current depths were not directly utilized in the hydraulic theory equations, and therefore the depth estimates provided by hydraulic theory and observations may be considered independent. The similarities between the observational and hydraulic theory values therefore provide reassurance that hydraulic theory describes the characteristics of these waves well for this case.

5. Discussion and conclusions

A packet of gravity waves formed in advance of a convectively generated density current during the nocturnal hours of 10 August 2014. Surface observations from the Oklahoma Mesonet and ARM networks were synthesized with vertical profiling observations from two AERIs and a DWL to analyze the spatiotemporal evolution of the density current and wave complex. The temporal evolution of the wave packet was primarily analyzed using the surface observation network, while the vertical profiling data were used to determine the vertical characteristics of the complex. The bore characteristics derived from hydraulic theory were compared to those derived from the observational analysis and provided a measure of the ability of the AERI and DWL to characterize the prebore environment.

Based on the observational analysis, the density current and gravity wave complex evolved as follows:

1) A convectively generated density current interacted with a statically stable, radiatively cooled boundary layer in northern Oklahoma within an environment favorable for ducting of southward-propagating waves. The primary contributor to wave ducting was the development of a pronounced low-level jet (Figs. 3–5, and 15).
2) A gravity wave developed as a result of the density current interacting with the surface-based inversion, but given that $\mu(=C_{gw}C_{dc}^{-1})$ was initially less than 0.7, there was initially very little separation between the bore and density current (Figs. 2 and 9a).
3) Numerous waves, initially of either Kelvin–Helmholtz or solitary wave form, developed behind the bore and were initially observed atop the density current (Fig. 9a).
4) The density current gradually became diffuse as it approached central Oklahoma, allowing the bore and trailing waves to separate from the current (Figs. 6, 7, and 9).
5) The gravity waves persisted throughout central Oklahoma and into southern Oklahoma. The waves trailing the bore exhibited characteristics of solitary waves once independent from the density current (i.e., the bore became undular). The solitary waves propagated within an elevated

inversion likely caused by 1) the vertical displacement of the surface-based inversion by the bore and 2) the relative compression of the atmosphere above the layer influenced by the bore (Figs. 10, 13, and 15).

6) As insolation destabilized the surface layer after sunrise, the wave complex eventually weakened and lost its bore characteristics in southern Oklahoma (Figs. 6 and 7).

While the wave complex closely resembled an undular bore, the presented case is distinct from previously documented undular bores in that the amplitude of the primary solitary wave is greater than the amplitude of the bore and the influence of the solitary waves did not extend to the surface. Further, the soliton itself was not amplitude ordered: the amplitude of the waves increased from the first to the fourth solitary waves, thereafter decreasing with each subsequent wave. The solitary waves did appear to originate from the bore, however, given that they propagated in a similar direction and appeared to continuously emanate from the bore based on radar observations.

There was no correlation between the near-surface mixing ratio and pressure tendencies resulting from bore passage, although a weak correlation (0.38) existed between near-surface temperature and pressure tendencies. While there appears to be no definitive theory proposed by previous studies explaining the correlation between the surface temperature and pressure perturbations, the following suggestion could be made—while speculative, a more thorough analysis is left for future work. As the bore strength increases, the total depth of the atmospheric column vertically displaced by the bore would also increase, which would allow for a greater amount of mass to be transported into the atmospheric column by the bore. Under the assumption that the mass is only displaced vertically and is then compressed through adiabatic cooling, the total mass in the atmospheric column would increase proportionally to the total amount of lifting induced by the bore. Because surface pressure is a measure of the quantity of mass in the atmospheric column, a greater increase in mass would lead to a greater surface pressure perturbation. Additionally, the magnitude of turbulence behind the bore head also increases with bore strength. Greater quantities of turbulence behind the bore head may then increase the amount of potentially warmer air mixed downward toward the surface, thereby increasing the surface temperature perturbation. Thus, the surface pressure and temperature perturbations would be correlated due to their similar dependence on bore strength.

The observed and computed bore and density current characteristics, where the latter were computed from hydraulic theory using AERI-retrieved thermodynamic profiles, agreed very well with relative absolute differences of less than 15%. The uncertainty in the AERI-retrieved profiles, including that associated with the decrease in the vertical resolution with height, had little impact on the accuracy of the hydraulic theory calculations since only observations in the nocturnal boundary layer, which was only 400 m deep, were required. Further, the uncertainties in the derived Scorer parameter profiles due to uncertainties in the AERI and DWL observations were negligible, suggesting that this instrument combination may be a robust option for future lower-tropospheric gravity wave analyses (see the appendixes).

While this case study offers unique insight into the physical characteristics of a wave packet consisting of a bore and trailing, elevated soliton, multiple questions remain that require further study, including the following: Of what significance is the lack of correlation between near-surface perturbations in mixing ratio and pressure in the current case, and does this characteristic extend to other cases? Of what significance are elevated solitons in initiating moist convection when propagating behind a bore?

Acknowledgments. Funding support for the National Weather Center instruments used in this study was provided by NSF MRI Grant AGS-1229181. We thank ARM for providing data gathered by the SGP instrument array. Insights offered by Dr. David Parsons and Kevin Haghi were invaluable to the development of this paper. We greatly appreciate the comments offered by the editor and anonymous reviewers.

APPENDIX A

Observational Error Analysis

The AERIoe-retrieved profiles of temperature and humidity include a full characterization of the uncertainty of each retrieval via the posterior covariance matrix (Turner and Löhnert 2014). While typically unimportant to the qualitative aspects of atmospheric profiles, small deviations in thermodynamic profiles may have a significant impact on the analysis of gravity wave environments [e.g., due to the dependence of gravity wave characteristics on inversion depth and magnitude as explained by Scorer (1949) and Crook (1988)]. Given that synoptic-scale conditions similar to those present for

TABLE A1. Error propagation terms and relative differences from Scorer parameter within ducting layers.

Variable	Term	Derived final form[a,b]	Log_{10} of relative diff
Temperature	σ_T^2	$g\left(\theta\frac{\partial^2\theta}{\partial z\partial T}-\frac{\partial\theta}{\partial T}\frac{\partial\theta}{\partial z}\right)[\theta^2(U-C)]^{-1}$	5.77 → 9.05
Wind speed	σ_V^2	$-2N^2\frac{\partial U}{\partial V}(U-C)^{-3}-\left[\frac{\partial^2}{\partial z^2}\left(\frac{\partial U}{\partial V}\right)(U-C)-\frac{\partial^2U}{\partial z^2}\frac{\partial U}{\partial V}\right](U-C)^{-2}$	1.16 → 4.71
Wind direction	σ_ϕ^2	$-2N^2\frac{\partial U}{\partial \phi}(U-C)^{-3}\left[\frac{\partial^2}{\partial z^2}\left(\frac{\partial U}{\partial \phi}\right)(U-C)-\frac{\partial^2U}{\partial z^2}\frac{\partial U}{\partial \phi}\right](U-C)^{-2}$	1.05 → 4.57
Bore speed	σ_C^2	$2N^2(U-C)^{-3}-\frac{\partial^2U}{\partial z^2}(U-C)^{-2}$	1.15 → 3.63
Bore direction	$\sigma_{\phi_{\text{prop}}}^2$	$-2N^2\frac{\partial U}{\partial \phi_{\text{prop}}}(U-C)^{-3}-\left[\frac{\partial^2}{\partial z^2}\left(\frac{\partial U}{\partial \phi_{\text{prop}}}\right)(U-C)-\frac{\partial^2U}{\partial z^2}\frac{\partial U}{\partial \phi_{\text{prop}}}\right](U-C)^{-2}$	2.01 → 4.49

[a] ϕ_{prop} is the direction of bore propagation, N is the Brunt–Väisälä frequency, and U is the wind component in the direction of bore movement.

[b] $\partial U/\partial V=\sin\phi\sin\phi_{\text{prop}}-\cos\phi\cos\phi_{\text{prop}}$, $\partial U/\partial\phi=V(\cos\phi\sin\phi_{\text{prop}}+\sin\phi\cos\phi_{\text{prop}})$, and $\partial U/\partial\phi_{\text{prop}}=V(\sin\phi\cos\phi_{\text{prop}}+\cos\phi\sin\phi_{\text{prop}})$.

this case would likely have been observed numerous times during the collection of the SGP radiosonde data used to generate the a priori database, the prebore atmospheric profiles retrieved by the AERI were likely representative of the actual atmospheric conditions [see sections 3a and 4b(1) for more information on the synoptic-scale conditions and prebore profiles, respectively]. However, due to the relative low frequency of bore and density current passages over the ARM SGP site, together with the relatively poor temporal resolution of the radiosondes launched there, the prior covariance matrix used in AERIoe does not well characterize the bore-influenced boundary layer and thus may lead to additional uncertainties in the AERIoe retrievals.

The propagation of AERI and DWL uncertainties through the Scorer parameter [l^2, Eq. (1)] was analyzed in an attempt to quantify the influences of the observational uncertainty on the presented analysis. Error propagation may be quantified as follows:

$$\sigma_{l^2}^2(T,V,\phi,C,\phi_{\text{prop}})=\sigma_T^2\left(\frac{\partial l^2}{\partial T}\right)^2+\sigma_V^2\left(\frac{\partial l^2}{\partial V}\right)^2+\sigma_\phi^2\left(\frac{\partial l^2}{\partial \phi}\right)^2+\sigma_C^2\left(\frac{\partial l^2}{\partial C}\right)^2+\sigma_{\phi_{\text{prop}}}^2\left(\frac{\partial l^2}{\partial \phi_{\text{prop}}}\right)^2, \quad \text{(A1)}$$

where σ is the standard deviation of the calculated variable, T is the ambient temperature, V is the horizontal wind speed, ϕ is the horizontal wind direction, C is the bore propagation speed, and ϕ_{prop} is the direction of bore propagation. We assumed that the uncertainties in the DWL-derived wind speed and direction were

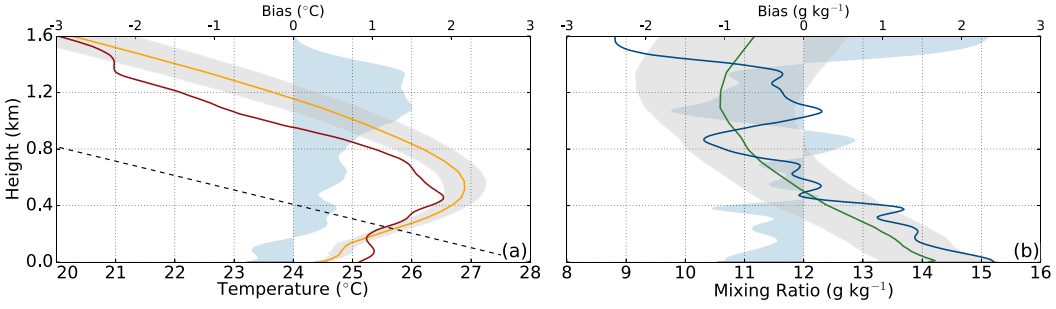

FIG. B1. Comparisons of vertical profiles of (a) temperature and (b) mixing ratio derived from radiosonde (red and blue, respectively) and AERI (yellow and green, respectively) data at Lamont at 0530 UTC 10 Aug 2014. Radiosonde data were derived from the 0530 UTC release for Lamont (actually released at 0533 UTC); AERI data were derived from the retrieval closest to the radiosonde release time. The gray shaded area around the vertical profiles denotes one standard deviation uncertainty from the mean AERI retrieval, as provided by the AERIoe retrieval algorithm. The blue shaded area about the center of the x axis denotes the bias of the AERI vertical profile relative to the radiosonde profile. The dashed black line in (a) denotes the dry adiabatic lapse rate.

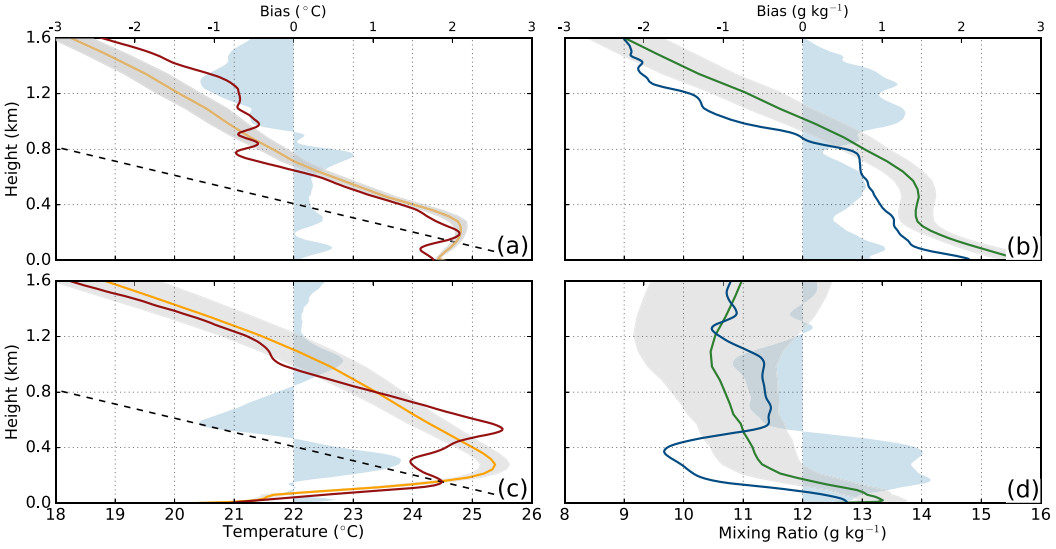

FIG. B2. As in Fig. B1, but for (a),(b) Norman and (c),(d) Lamont at 1200 UTC. Radiosonde data were derived from the 1200 UTC releases for both Norman and Lamont (actually released at 1102 and 1126 UTC, respectively); AERI data were derived from the retrieval closest to the radiosonde release time.

constant values of 0.05 m s^{-1} and 10°, respectively. Error values of AERI observations were provided by the AERIoe algorithm, and included contributions from the uncertainty of the AERI radiance observations, the sensitivity of the forward model, and the uncertainty of the prior dataset used to constrain the retrieval.

The uncertainty in the Scorer parameter due to uncertainties in the DWL and AERI observations was at least one order of magnitude smaller than the Scorer parameter within the ducting layers (Table A1). At most, this might result in a negligible (<10 m) erroneous vertical displacement of heights where the Scorer parameter transitioned between positive and negative values. We therefore conclude that the uncertainties of the remote sensors are insignificant for the analysis of this case.

APPENDIX B

AERI-Specific Errors

Vertical profiles of temperature and water vapor retrieved from the AERI radiance spectra were compared to a prebore radiosonde (released at 0530 UTC at Lamont) and two postbore radiosonde releases (1200 UTC at Lamont and Norman) (Figs. B1 and B2). Of note, the prebore radiosonde mixing ratio profile from Lamont at 0530 UTC appears to be erroneous based on the frequent mixing ratio fluctuations in the well-mixed layer (deduction based on the adiabatic temperature profile) between approximately 700 and 1300 m (Fig. B1). The mixing ratio profile was therefore neglected for this instance, and only the temperature profile was considered.

The qualitative features important to the deduction of environments favorable for bore generation and maintenance, such as the presence of a surface-based inversion, were captured appropriately by the AERI, although small-scale features were not. Elevated inversions present in both the Norman (Figs. B2a,b) and Lamont (Figs. B2c,d) postbore radiosonde data were not present in the AERI-retrieved temperature profiles. Using only the AERI data, the nature of the elevated inversion and any associated elevated gravity waves would be uncertain; however, by including DWL and/or radiosonde data into the analysis, regions favorable for elevated gravity wave propagation are more easily and accurately identified. This suggests complementing the AERI with a DWL is beneficial for postbore profiling to ensure elevated inversions and the resulting ducting layers are more likely to be captured.

REFERENCES

Benjamin, T. B., and M. J. Lighthill, 1954: On cnoidal waves and bores. *Proc. Roy. Soc. London*, **224**, 448–460, doi:10.1098/rspa.1954.0172.

Brock, F., K. Crawford, R. Elliott, G. Cuperus, S. Stadler, H. Johnson, and M. Eilts, 1995: The Oklahoma Mesonet: A technical overview. *J. Atmos. Oceanic Technol.*, **12**, 5–19, doi:10.1175/1520-0426(1995)012<0005:TOMATO>2.0.CO;2.

Christie, D. R., K. J. Muirhead, and A. L. Hales, 1979: Intrusive density flows in the lower troposphere: A source of atmospheric solitons. *J. Geophys. Res.*, **84**, 4959–4970, doi:10.1029/JC084iC08p04959.

Clarke, R. H., R. K. Smith, and D. G. Reid, 1981: The Morning Glory of the Gulf of Carpentaria: An atmospheric undular bore. *Mon. Wea. Rev.*, **109**, 1726–1750, doi:10.1175/1520-0493(1981)109<1726:TMGOTG>2.0.CO;2.

Coleman, T. A., and K. R. Knupp, 2011: Radiometer and profiler analysis of the effects of a bore and a solitary wave on the stability of the nocturnal boundary layer. *Mon. Wea. Rev.*, **139**, 211–223, doi:10.1175/2010MWR3376.1.

——, ——, and D. Herzmann, 2009: The spectacular undular bore in Iowa on 2 October 2007. *Mon. Wea. Rev.*, **137**, 495–503, doi:10.1175/2008MWR2518.1.

Crook, N. A., 1986: The effect of ambient stratification and moisture on the motion of atmospheric undular bores. *J. Atmos. Sci.*, **43**, 171–181, doi:10.1175/1520-0469(1986)043<0171:TEOASA>2.0.CO;2.

——, 1988: Trapping of low-level internal gravity waves. *J. Atmos. Sci.*, **45**, 1533–1541, doi:10.1175/1520-0469(1988)045<1533:TOLLIG>2.0.CO;2.

Droegemeier, K. K., and R. B. Wilhelmson, 1987: Numerical simulation of thunderstorm outflow dynamics. Part I: Outflow sensitivity experiments and turbulence dynamics. *J. Atmos. Sci.*, **44**, 1180–1210, doi:10.1175/1520-0469(1987)044<1180:NSOTOD>2.0.CO;2.

Feltz, W., W. Smith, H. Howell, R. Knuteson, H. Woolf, and H. Revercomb, 2003: Near-continuous profiling of temperature, moisture, and atmospheric stability using the atmospheric emitted radiance interferometer (AERI). *J. Appl. Meteor.*, **42**, 584–597, doi:10.1175/1520-0450(2003)042<0584:NPOTMA>2.0.CO;2.

Fritts, D. C., and P. K. Rastogi, 1985: Convective and dynamical instabilities due to gravity wave motions in the lower and middle atmosphere: Theory and observations. *Radio Sci.*, **20**, 1247–1277, doi:10.1029/RS020i006p01247.

Geerts, B., and Coauthors, 2017: The 2015 Plains Elevated Convection at Night field project. *Bull. Amer. Meteor. Soc.*, **98**, 767–786, doi:10.1175/BAMS-D-15-00257.1.

Goler, R. A., and M. J. Reeder, 2004: The generation of the Morning Glory. *J. Atmos. Sci.*, **61**, 1360–1377, doi:10.1175/1520-0469(2004)061<1360:TGOTMG>2.0.CO;2.

Haase, S. P., and R. K. Smith, 1984: Morning Glory wave clouds in Oklahoma: A case study. *Mon. Wea. Rev.*, **112**, 2078–2089, doi:10.1175/1520-0493(1984)112<2078:MGWCIO>2.0.CO;2.

——, and ——, 1989: The numerical simulation of atmospheric gravity currents. Part I: Neutrally-stable environments. *Geophys. Astrophys. Fluid Dyn.*, **46**, 1–33, doi:10.1080/03091928908208902.

Hartung, D. C., J. A. Otkin, J. E. Martin, and D. D. Turner, 2010: The life cycle of an undular bore and its interaction with a shallow, intense cold front. *Mon. Wea. Rev.*, **138**, 886–908, doi:10.1175/2009MWR3028.1.

Karan, H., and K. Knupp, 2009: Radar and profiler analysis of colliding boundaries: A case study. *Mon. Wea. Rev.*, **137**, 2203–2222, doi:10.1175/2008MWR2763.1.

Karyampudi, V. M., S. E. Koch, C. Chen, J. W. Rottman, and M. L. Kaplan, 1995: The influence of the Rocky Mountains on the 13–14 April 1986 severe weather outbreak. Part II: Evolution of a prefrontal bore and its role in triggering a squall line. *Mon. Wea. Rev.*, **123**, 1423–1446, doi:10.1175/1520-0493(1995)123<1423:TIOTRM>2.0.CO;2.

Kingsmill, D. E., and N. A. Crook, 2003: An observational study of atmospheric bore formation from colliding density currents. *Mon. Wea. Rev.*, **131**, 2985–3002, doi:10.1175/1520-0493(2003)131<2985:AOSOAB>2.0.CO;2.

Klazura, G. E., and D. A. Imy, 1993: A description of the initial set of analysis products available from the NEXRAD WSR-88D system. *Bull. Amer. Meteor. Soc.*, **74**, 1293–1311, doi:10.1175/1520-0477(1993)074<1293:ADOTIS>2.0.CO;2.

Knupp, K., 2006: Observational analysis of a gust front to bore to solitary wave transition within an evolving nocturnal boundary layer. *J. Atmos. Sci.*, **63**, 2016–2035, doi:10.1175/JAS3731.1.

Knuteson, R. O., and Coauthors, 2004a: Atmospheric Emitted Radiance Interferometer. Part I: Instrument design. *J. Atmos. Oceanic Technol.*, **21**, 1763–1776, doi:10.1175/JTECH-1662.1.

——, and Coauthors, 2004b: Atmospheric Emitted Radiance Interferometer. Part II: Instrument performance. *J. Atmos. Oceanic Technol.*, **21**, 1777–1789, doi:10.1175/JTECH-1663.1.

Koch, S. E., and W. L. Clark, 1999: A nonclassical cold front observed during COPS-91: Frontal structure and the process of severe storm initiation. *J. Atmos. Sci.*, **56**, 2862–2890, doi:10.1175/1520-0469(1999)056<2862:ANCFOD>2.0.CO;2.

——, P. B. Dorian, R. Ferrare, S. H. Melfi, W. C. Skillman, and D. Whiteman, 1991: Structure of an internal bore and dissipating gravity current as revealed by Raman lidar. *Mon. Wea. Rev.*, **119**, 857–887, doi:10.1175/1520-0493(1991)119<0857:SOAIBA>2.0.CO;2.

——, W. Feltz, F. Fabry, M. Pagowski, B. Geerts, K. M. Bedka, D. O. Miller, and J. W. Wilson, 2008a: Turbulent mixing processes in atmospheric bores and solitary waves deduced from profiling systems and numerical simulation. *Mon. Wea. Rev.*, **136**, 1373–1400, doi:10.1175/2007MWR2252.1.

——, C. Flamant, J. W. Wilson, B. M. Gentry, and B. D. Jamison, 2008b: An atmospheric soliton observed with Doppler radar, differential absorption lidar, and a molecular Doppler lidar. *J. Atmos. Oceanic Technol.*, **25**, 1267–1287, doi:10.1175/2007JTECHA951.1.

Locatelli, J. D., M. T. Stoelinga, and P. V. Hobbs, 2002: A new look at the super outbreak of tornadoes on 34 April 1974. *Mon. Wea. Rev.*, **130**, 1633–1651, doi:10.1175/1520-0493(2002)130<1633:ANLATS>2.0.CO;2.

Lundquist, J. K., M. J. Churchfield, S. Lee, and A. Clifton, 2015: Quantifying error of lidar and sodar Doppler beam swinging measurements of wind turbine wakes using computational fluid dynamics. *Atmos. Meas. Tech.*, **8**, 907–920, doi:10.5194/amt-8-907-2015.

Martin, E. R., and R. H. Johnson, 2008: An observational and modeling study of an atmospheric internal bore during NAME 2004. *Mon. Wea. Rev.*, **136**, 4150–4167, doi:10.1175/2008MWR2486.1.

McPherson, R., and Coauthors, 2007: Statewide monitoring of the mesoscale environment: A technical update on the Oklahoma Mesonet. *J. Atmos. Oceanic Technol.*, **24**, 301–321, doi:10.1175/JTECH1976.1.

Nasr-Azadani, M. M., and E. Meiburg, 2015: Gravity currents propagating into shear. *J. Fluid Mech.*, **778**, 552–585, doi:10.1017/jfm.2015.398.

Pearson, G., F. Davies, and C. Collier, 2009: An analysis of the performance of the UFAM pulsed Doppler lidar for observing the boundary layer. *J. Atmos. Oceanic Technol.*, **26**, 240–250, doi:10.1175/2008JTECHA1128.1.

Rottman, J. W., and J. E. Simpson, 1989: The formation of internal bores in the atmosphere: A laboratory model. *Quart. J. Roy. Meteor. Soc.*, **115**, 941–963, doi:10.1002/qj.49711548809.

——, and F. Einaudi, 1993: Solitary waves in the atmosphere. *J. Atmos. Sci.*, **50**, 2116–2136, doi:10.1175/1520-0469(1993)050<2116:SWITA>2.0.CO;2.

——, and R. Grimshaw, 2002: Atmospheric internal solitary waves. *Environmental Stratified Flows*, R. Grimshaw, Ed., Springer, 61–88, doi:10.1007/0-306-48024-7_3.

Scorer, R. S., 1949: Theory of waves in the lee of mountains. *Quart. J. Roy. Meteor. Soc.*, **75**, 41–56, doi:10.1002/qj.49707532308.

Sheng, C., M. Xue, and S. Gao, 2009: The structure and evolution of sea breezes during the Qingdao Olympics sailing test event in 2006. *Adv. Atmos. Sci.*, **26**, 132–142, doi:10.1007/s00376-009-0132-y.

Sisterson, D. L., R. A. Peppler, T. S. Cress, P. J. Lamb, and D. D. Turner, 2016: *The ARM Southern Great Plains (SGP) Site*. *Meteor. Monogr.*, No. 57, Amer. Meteor. Soc., 6.1–6.14, doi:10.1175/AMSMONOGRAPHS-D-16-0004.1.

Smith, R. K., G. Roff, and N. Crook, 1982: The Morning Glory: An extraordinary atmospheric undular bore. *Quart. J. Roy. Meteor. Soc.*, **108**, 937–956, doi:10.1002/qj.49710845813.

Stokes, G. M., and S. E. Schwartz, 1994: The Atmospheric Radiation Measurement (ARM) program: Programmatic background and design of the cloud and radiation test bed. *Bull. Amer. Meteor. Soc.*, **75**, 1201–1221, doi:10.1175/1520-0477(1994)075<1201:TARMPP>2.0.CO;2.

Turner, D. D., and U. Löhnert, 2014: Information content and uncertainties in thermodynamic profiles and liquid cloud properties retrieved from the ground-based Atmospheric Emitted Radiance Interferometer (AERI). *J. Appl. Meteor. Climatol.*, **53**, 752–771, doi:10.1175/JAMC-D-13-0126.1.

——, R. O. Knuteson, H. E. Revercomb, C. Lo, and R. G. Dedecker, 2006: Noise reduction of Atmospheric Emitted Radiance Interferometer (AERI) observations using principal component analysis. *J. Atmos. Oceanic Technol.*, **23**, 1223–1238, doi:10.1175/JTECH1906.1.

Wakimoto, R. M., and D. E. Kingsmill, 1995: Structure of an atmospheric undular bore generated from colliding boundaries during CaPE. *Mon. Wea. Rev.*, **123**, 1374–1393, doi:10.1175/1520-0493(1995)123<1374:SOAAUB>2.0.CO;2.

Watson, C. D., and T. P. Lane, 2016: A case of an undular bore and prefrontal precipitation in the Australian Alps. *Mon. Wea. Rev.*, **144**, 2623–2644, doi:10.1175/MWR-D-15-0355.1.